Available online at www.sciencedirect.com
SCIENCE DIRECT®
International Journal of Heat and Mass Transfer 48 (2005) 4243–4264
International Journal of HEAT and MASS TRANSFER
www.elsevier.com/locate/ijhmt

Contribution of vortex structures and flow separation to local and overall pressure and heat transfer characteristics in an ultralightweight lattice material

T. Kim [a], H.P. Hodson [b], T.J. Lu [b,c,*]

[a] School of Mechanical and Aerospace Engineering, Seoul National University, Republic of Korea
[b] Department of Engineering, University of Cambridge, UK
[c] School of Aerospace, Xian Jiaotong University, Xian 710049, PR China

Received 18 February 2004

Abstract

Ultralightweight lattice-frame materials (LFMs) with open, periodic microstructures are attractive multifunctional systems that can perform structural, thermal, actuation, power storage and other functions [A.G. Evans, J.W. Hutchinson, M.F. Ashby, Multifunctionality of cellular metal systems, Prog. Mater. Sci. 43 (1999) 171–221]. This paper presents experimental and numerical studies of local fluid flow behaviour and its contribution to local and overall pressure and heat transfer characteristics of such a lattice material with tetrahedral unit cells. A single layer of the LFM with porosity of 0.938 is sandwiched between impermeable endwalls that receive uniform heat flux and the heat transfer is subjected to forced air convection.

Experimental measurements with particle image velocity (PIV) and thermochromic liquid crystal (TLC), backed by computational fluid mechanics (CFD) simulations, revealed two dominant local flow features in the LFM. Distinctive vortex structures near the vertices where the LFM meets the endwalls and flow separation on the surface of LFM struts were observed. The vortex structures formed around the vertices include horseshoe vortices and arch-shaped vortices. The horseshoe vortex increases local heat transfer on the endwall region up to 180% more than that in regions where the least influence of the horseshoe vortex is present. The arch-shaped vortex behind the vertices creates regions of flow recirculation and reattachment, leading to relatively high heat transfer.

The location of flow separation along the struts varies with the spanwise position due to the presence of vertices (or endwalls). The regions on the strut surface before flow separation contribute approximately 40% of the total heat transfer in the LFM. The delay of the flow separation leads to an increase in the overall heat transfer.

Comparisons with foams and other heat dissipation media such as packed beds, louvered fins and microtruss materials suggest that the LFMs compete favourably with the best available heat dissipation media.

* Corresponding author. Address: School of Aerospace, Xian Jiaotong University, Xian 710049, PR China.
E-mail address: tjlu@mail.xjtu.edu.cn (T.J. Lu).

0017-9310/$ - see front matter © 2005 Elsevier Ltd. All rights reserved.
doi:10.1016/j.ijheatmasstransfer.2005.04.026

Nomenclature

c_p	specific heat at constant pressure [J/kg K]	P	static pressure [P]
C_p	static pressure coefficient ($=(P - P_{\text{cell-inlet}})/(\rho U^2/2)$)	q	heat flux ($=Q/A$) [W/m^2]
		Q	heat flow [W]
d	strut diameter [m]	Re_{d_p}	Reynolds number ($=\rho U d_p/\mu$)
d_p	unit cell length (or longitudinal unit cell pitch) [m]	S	spacing between struts [m]
		t	time [s]
h	convective heat transfer coefficient [W/m^2 K]	T	temperature [K]
		U	mean flow velocity [m/s]
H, W, L	height, width and length of test section [m]	x, y, z	coordinates
k	thermal conductivity [W/m K]	z'	coordinate along the strut
K_{Cell}	pressure loss coefficient ($=(\Delta P/L)d_p/(\rho U^2/2)$)	ρ_{SA}	surface area density (=surface area/volume) [m^{-1}]
l	strut length [m]		
$\dot{m}$	mass flow rate [kg/s]	ε	porosity
Nu_{d_p}	Nusselt number ($=hd_p/k_f$)		

1. Introduction

The rapid advance in manufacturing techniques (e.g. lithography and rapid prototyping) has made possible the construction of lightweight, highly porous cellular metal systems with pre-specified periodic microstructures. The precise control of topologies during the manufacturing stage differentiates these novel cellular materials from conventional porous heat dissipation media such as metal foams with stochastic microstructures.

The periodic cellular structures were primarily used by the materials and structures community owing to the flexibility in design and their superior mechanical strength/stiffness to stochastic structures. Well established data on the mechanical properties of cellular systems with either periodic or stochastic microstructures can be found in [1–6]. These studies demonstrate that the relatively high stiffness and yield strength achievable at low density creates an opportunity for lightweight structures. In addition, the open topologies with high surface area density have thermal attributes that may enable applications which require a structure for heat dissipation as well as mechanical stiffness/strength.

The focus of this work is on one of the periodic cellular materials made possible by computer-based design and numerically controlled processing, namely lattice-frame material (LFM). The LFM consists of a three-dimensional network of cylindrical struts forming a tetrahedron as shown in Fig. 1(a). This tetrahedral unit cell is interconnected with other unit cells, which are periodically and spatially distributed (see Fig. 1(b)).

The overall pressure loss and heat transfer performance of the LFM were reported in [7], whilst its detailed pressure loss and heat transfer behaviour were examined in [8–10]. It was found that the orientation of the LFM has a strong effect on flow resistance but not on heat transfer. In addition to promote flow mixing, LFM struts made with a high thermal conductivity material (e.g. aluminium) enhance overall heat dissipation by conduction through solid struts followed by convection from strut surfaces. In comparison, LFM struts made with a low conducting material (e.g. polycarbonate) contribute to heat transfer by means of flow mixing only. It was also revealed that the overall pressure loss of flow across the LFM is dominated by pressure drag for the Reynolds number considered.

To complete the study of thermofluid characteristics in the LFM heat dissipation medium under forced air cooling, this paper aims to (1) identify governing local flow features; (2) examine the contribution of these features to the local pressure and heat transfer distribution; (3) quantify their influence on the overall thermal and hydraulic performance; and (4) compare the performance of LFMs with selected porous heat dissipation media including metal foams, packed beds and louvered fins. Experimental measurements with particle image velocimetry (PIV) and thermochromic liquid crystal (TLC), complemented by CFD simulation, are carried out. To examine the detailed local flow and heat transfer features, a LFM model much larger than the LFM structures studied in [7–10] is fabricated and tested.

2. Experimental apparatus and procedure

2.1. Test rig

A test rig that accommodated a single layered LFM model was fabricated; its photograph is given in Fig. 2. An axial fan draws the flow and mass flow rate in the test section can be varied. A flow straightener (honeycomb) was placed after a bell-mouth shaped inlet. This was followed by a 500 mm long parallel section.

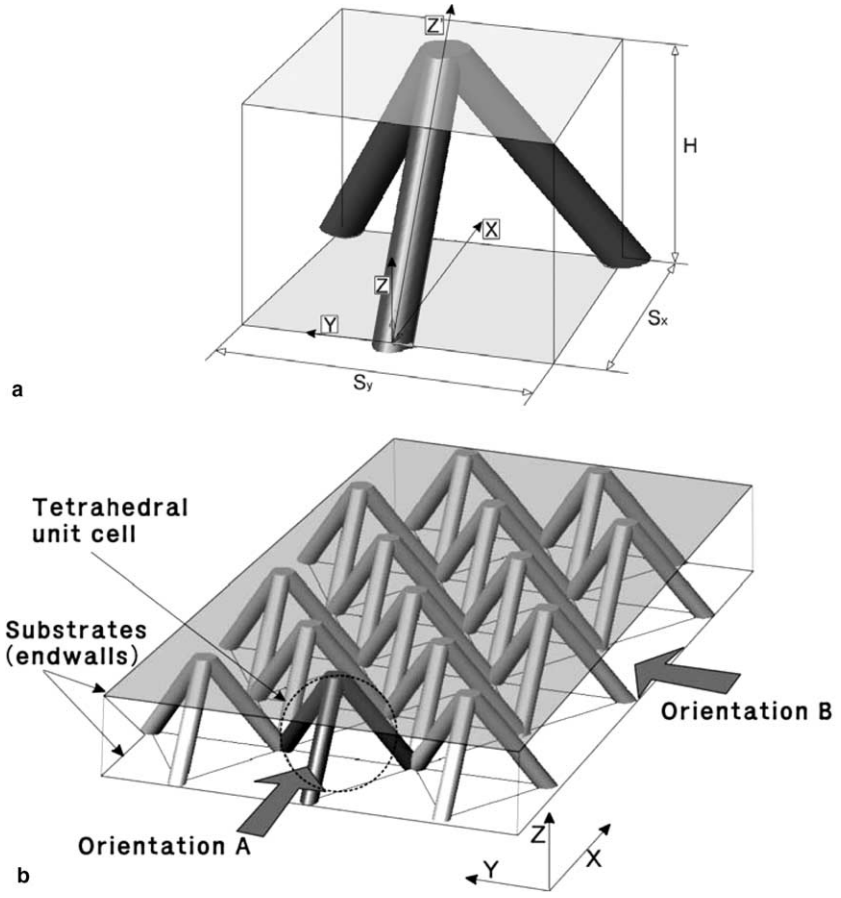

Fig. 1. Topology of LFM: (a) a tetrahedral unit cell; (b) a single layered LFM sandwiched between face sheets, showing structural anisotropy.

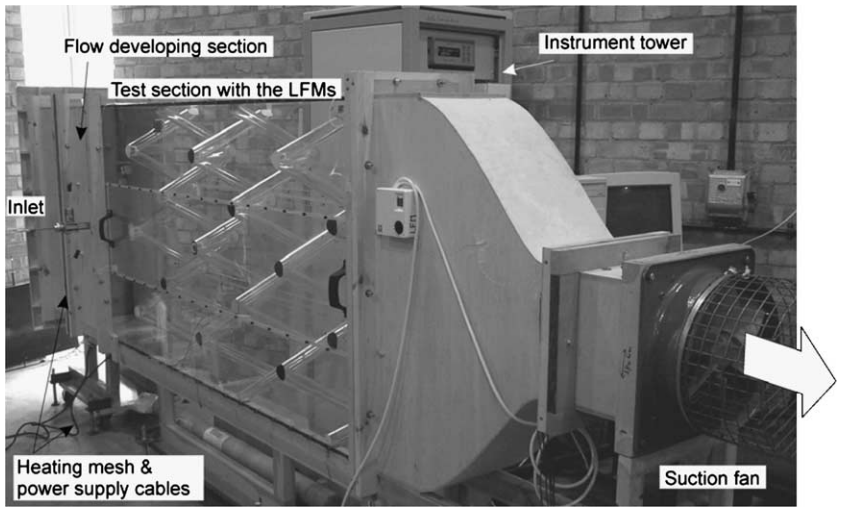

Fig. 2. Photograph of test rig used to obtain detailed fluid-flow and heat transfer patterns.

Table 1
Specifications of the wind-tunnels employed for both pressure drop and heat transfer measurements where $L_{parallel}$ is a length of the parallel section and H, W, L and are the channel height, width, and length, respectively

	Test rig
Flow straighter (honeycomb)	1
Parallel section ratio ($L_{parallel}/H$)	2
Test section ($H \times W \times L$) [m]	$0.270 \times 0.993 \times 1.72$
Heating mesh ($H \times W$) [m]	0.270×0.993
Number of unit cells	3 (transverse) × 6 (longitudinal)
Type of air supply	Suction type single axial fan

During the data reduction process associated with transient heat transfer experiments using thermochromic liquid crystal (TLC), a 1D semi-infinite solid assumption (discussed in Section 2.4) which requires a step input of the flow temperature change is typically used. To provide the step input, a heating mesh was fabricated, following the methods reported in [11]. The heating mesh was inserted between the parallel section and another parallel section (500 mm long) before the test section. It was made of stainless steel wire of 36 μm diameter and was sandwiched between two Túfnol frames after being soldered to brass bus bars. The bus bars are used to connect the heating mesh to a low voltage and high current transformer. While air is passing through the heating mesh, the heat generated by the electrical current is transferred to the air. The heating mesh was connected to an AC welding power transformer that was able to supply a high current from 40 A up to 250 A. Specifications of the test rig are tabulated in Table 1.

2.2. LFM test model

In the test section, 18 tetrahedral unit cells were located. There were 3 and 6 unit cells in the transverse and longitudinal directions, respectively. Only two unit cells from the centre of the test model were selected as the region of interest for the TLC experiment.

The struts of the test model were fabricated from Perspex tubes with a wall thickness of 6 mm and an outer diameter of 45 mm. The ends of each strut were machined to fit with other struts. During the assembly of the machined struts to construct the tetrahedral LFM, chloroform was used to fix all except the removable struts used later for the pressure distribution measurements (see Section 2.3). The ratio of strut length to diameter was 7.35. The model has a porosity of 0.938 when the struts are solid, where 'porosity' is defined as the void volume fraction to the total volume that is occupied by the inserted structures, e.g., the LFM [14]. Strut diameter, length and cell height are 0.045 m, 0.331 m, and 0.27 m, respectively. The Perspex test model is approximately 20 times larger than the aluminium alloy LFM structures tested in [7–10].

2.3. Pressure and velocity measurements

2.3.1. Pressure loss and pressure distribution

Static pressure tappings were installed in the inlet and outlet sections of the test section. The static pressure tappings were connected to a 48 port J-type Scanivalve™. Because the velocity range in the test rig was 0.5–1.5 m/s, in order to match Reynolds numbers with those in the small scale LFM model tests [7,9], an analogue manometer (MDC FC001, Furness Controls), which has a pressure reading resolution of about 0.1 P, was connected to the Scanivalve™. The output from the analogue pressure signals was sent to an A/D card inserted in the data acquisition PC. The LabVIEW™ software monitored and stored the pressure data.

Pressure distributions around the circumference of the struts were measured. The measurements were carried out for a unit cell, located at the centre of the LFM matrix, i.e., the third cell out of six cells in the longitudinal direction (x-axis). A static pressure tapping ring consisting of 24 tappings with 15° increments along its circumference was fabricated as shown in Fig. 3. To traverse the measuring location along the strut span, the ring was swapped with a neighbouring plane tube ring; a total of 15 stages were used during the measurements.

2.3.2. Velocity field measurements

To observe velocity field around the LFM structures, the PIV technique was used. A schematic of a measured plane is given in Fig. 4. The result is also used to validate CFD simulation results (see Section 3). The PIV is capable of measuring the velocity field in a plane by determining the displacement of illuminated particles over a short interval of time using a double-pulsed light source.

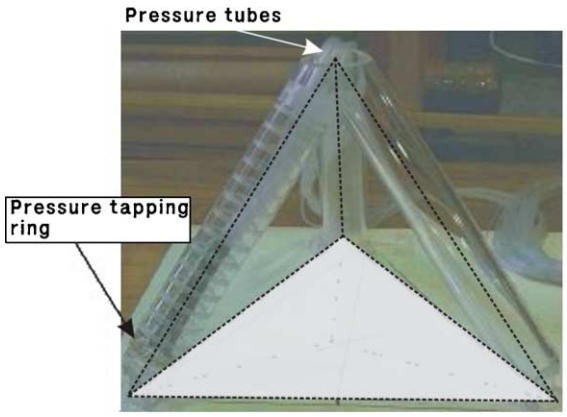

Fig. 3. Photograph of the pressure tapping ring installed.

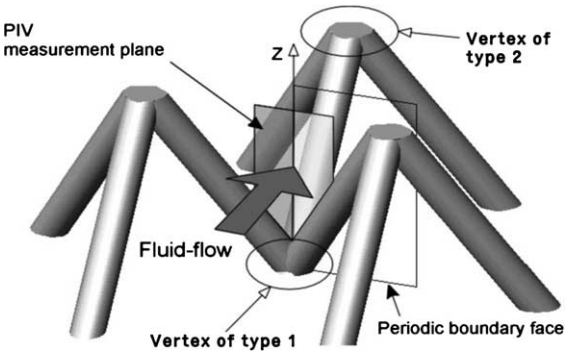

Fig. 4. Transverse plane used for PIV velocity measurements.

A Nd:YAG laser was used in this study. Details associated with the PIV experiment can be found in Ref. [8].

2.3.3. Flow visualisation using the oil–florescent dye mixture technique

An oil–florescent dye mixture technique was used to carry out flow visualisation on the LFM strut (for the large model used in this study) and endwall surfaces (for the small scale model reported in [9]). The latter model also has the same porosity of 0.938 and scaled down to have a ratio of 1:22.5 with respect to the model used in the present study. The experiment involves covering the strut and endwall surfaces with a fluorescent powder and oil mixture so that when aerodynamic forces exert on the surfaces, shear stresses redistribute the mixture patterns, resulting in the visualisation of the surface flow patterns. Before the mixture was coated on selected surfaces, the strut tube was painted in black. This black background was used to enhance the reflectivity when using ultraviolet light to illuminate the surface flow pattern while it was being photographed.

2.4. Transient heat transfer measurement using thermochromic liquid crystal

2.4.1. Image acquisition setup and procedure

To obtain detailed surface heat transfer mapping on endwalls, thermochromic liquid crystal (TLC) technique was used. Two separate heat transfer experiments were conducted on the endwall surface and the strut surfaces. The solution of the encapsulated liquid crystals (BM/R27C6W/C17-10, Hallcrest Inc.), premixed binder and de-ionised water was sprayed using an airbrush. Subsequently, the black backing paint (BB-G1, Hallcrest Inc.) was sprayed on top of the TLC layer. The illumination source used here provides low thermal radiation with continuous cold-white light (Intralux dc-1100, Volpi Inc.).

Instrumentation used for curved surface (i.e. strut surface) needed additional equipment. This is due to the structural complexity and the need to prevent flow disturbances caused by the insertion of a lighting source and an image capturing system into the flow. A borescope (R060-046-045SW115-50, Olympus Inc.) was employed, which is an optical device allowing one to monitor images through a long and small diameter metallic tube (6 mm in diameter and 450 mm in length). A digital camcorder (SONY DCR-PC110E) connected to the borescope was mounted on a traverse system as shown in Fig. 5(a). It allows a linear traverse of 400 mm as well as 360° rotation of the viewing lens of the borescope. There is a swing prism system so that direct reflection from the illumination by the internal light source can be avoided. Fig. 5(b) shows the internal light source and the borescope lens. The light source was connected to the main light generator (KMI MLS-201) by a fibre optic. The borescope was therefore used to observe the reflected light from the TLC layer sprayed on the outer surface of the strut tube. It monitored the TLC colour display from the inside of the strut tube, looking through the tube thickness (6 mm).

During the transient experiments, the colour changes of the reflected light of the TLC on the target surface

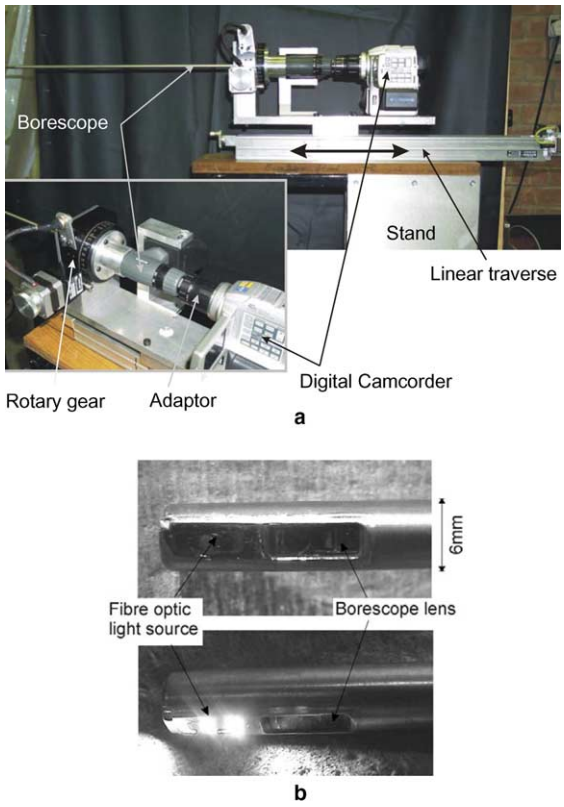

Fig. 5. Photograph of borescope setup to monitor the color change of the liquid crystal coated on outer surface of cylinder tube; it captures images from within the tube.

were monitored using the digital camera. The camera was connected to an image acquisition PC via an IEEE 1394 (Firewire™) for real time recording. The images were saved in PAL format (25 frames per second). During data processing, the TLC images in the RGB space were converted into HSI (Hue, Saturation and Intensity) space using the IMAQ™ software from National Instrument Inc., which is part of LabVIEW™. The hue values of the images are then converted into temperatures based on calibration between hue value and temperature.

2.4.2. Determination of the heat transfer coefficient in the TLC

During the transient heat transfer experiments reported here, the air temperature increases exponentially with time. When normalized, this is described by the expression:

$$\Theta_{\mathrm{f}}(t) = \frac{T_{\mathrm{f}}(t) - T_{\mathrm{init}}}{T_{\mathrm{final}} - T_{\mathrm{init}}} = 1 - \mathrm{e}^{-t/\tau_2} \tag{1}$$

where t is the time, $T_{\mathrm{f}}(t)$ is the fluid temperature which varies with time (t), τ_2 is the time constant, T_{final} is the final (or target) fluid temperature, and T_{init} is the initial fluid temperature. As reported in [12], τ_2 decreases steeply as the flow velocity is increased for a given power input to the heating mesh. The exponential rise of the flow temperature, instead of the ideal step rise, means that the 1D semi-infinite equation for the step rise of the flow temperature must be modified. It is replaced by the solution for an exponential increase according to [13].

The solid temperature T_{s} at a fixed position (x, y) on the surface of the endwall (treated as a semi-infinite solid) when the flow temperature at the same location exhibits an exponential rise may be written as

$$\begin{aligned}\frac{T_{\mathrm{s}}(t) - T_{\mathrm{init}}}{T_{\mathrm{final}} - T_{\mathrm{init}}} &= 1 - \frac{1}{1+\beta_{\tau_2}^2}\mathrm{e}^{\beta^2}\mathrm{erfc}(\beta) \\ &\quad - \mathrm{e}^{-t/\tau_2}\frac{\beta_{\tau_2}^2}{1+\beta_{\tau_2}^2}\left\{1 + \frac{1}{\beta_{\tau_2}}\left[\frac{1}{\pi}\sqrt{\frac{t}{\tau_2}}\right.\right. \\ &\quad \left.\left. + \frac{2}{\pi}\sum_{n=1}^{\infty}\frac{1}{n}\mathrm{e}^{-n^2/4}\sinh\left(n\sqrt{\frac{t}{\tau_2}}\right)\right]\right\}\end{aligned} \tag{2}$$

where $\beta = h\sqrt{\alpha t}/k_{\mathrm{s}}$, $\beta_{\tau_2} = h\sqrt{\alpha\tau_2}/k_{\mathrm{s}}$, h is the heat transfer coefficient, α is a thermal diffusivity of the solid, k_{s} is a thermal conductivity of the solid, and τ_2 is the time constant that depends on the performance of the heating mesh.

Since the non-dimensional temperature can be obtained from measured $T_{\mathrm{s}}(t)$ by the TLC, the heat transfer coefficient, h, which is the only unknown in Eq. (2), can be implicitly calculated by comparing the non-dimensional temperature from the TLC experiments and that predicted from Eq. (2).

2.5. Data reduction

2.5.1. Pressure loss coefficient (pressure drop per unit cell)

In periodic structures such as the LFM, it is expected that the flow patterns will also be periodic, excluding any entry and exit regions [9]. This fact leads to the consideration of a unit cell for pressure drop and heat transfer analyses. Information concerning the representative unit cell can then be utilised to predict the performance of the overall structure.

In an isotropic structure, one characteristic length scale is normally sufficient to represent the structure under unidirectional flow conditions. However, in an anisotropic structure such as the LFM, it is necessary to determine a characteristic length, d_p according to the orientation of the structure relative to the flow direction. This is because variations of flow blockage and geometry of flow passage exist even though the porosity of the structure remains unchanged. For the current study, two orientations such as Orientation A (O-A) and Orientation B (O-B) were selected: Fig. 1(b) illustrates the difference of the unit cell length for each orientation.

The pressure loss coefficient K_{Cell} representing the pressure drop across the unit cell length d_p is defined as

$$K_{\mathrm{Cell}} = \frac{\Delta P_{\mathrm{Cell}}}{\rho U^2/2}$$

where ΔP_{Cell} is a static pressure drop per unit cell length ($=(\Delta P/L)d_p$), $\Delta P/L$ is the pressure drop per unit length, and $\rho U^2/2$ is a dynamic pressure based on the mean inlet velocity, U, and d_p is the unit cell length.

To calculate the overall pressure loss across the LFM matrix, K_{Cell} would be multiplied by the total number of unit cells in the flow direction. It should be noted that the pressure loss coefficient does not account for the entry and exit effects that occur.

2.5.2. Static pressure coefficient, C_p

To evaluate the local pressure distribution on the strut surfaces, a non-dimensional static pressure coefficient is defined as

$$C_p = \frac{P(\varphi) - P_{\text{cell-inlet}}}{\rho U^2/2}$$

where $P(\varphi)$ is the static pressure measured along the strut circumference, φ is the azimuth angle measured from the stagnation point, and $P_{\text{cell-inlet}}$ is a representative static pressure at the inlet of unit cell calculated as

$$P_{\text{cell-inlet}} = P_{\text{inlet}} - K_{\mathrm{Cell}}N\left(\frac{\rho U^2}{2}\right)$$

where P_{cell} is the measured static pressure at the inlet of the test section, K_{Cell} is the pressure loss coefficient and N is the number of cells between the inlet and the unit cell of interest.

The Reynolds number based on the unit cell length is defined as

$$Re_{d_p} = \frac{\rho U d_p}{\mu}$$

where μ is the viscosity of the fluid.

2.5.3. Heat transfer coefficient and Nusselt number in TLC measurements

The local heat transfer coefficient $h(x,y)$ on the endwall calculated using Eq. (2) together with the TLC measurements was averaged over the endwall surface area to obtain spatially averaged heat transfer coefficient h as

$$h = \int_y \int_x h(x,y)\,\mathrm{d}x\,\mathrm{d}y$$

The overall Nusselt number, Nu_{d_p}, is then defined as

$$Nu_{d_p} = \frac{h}{k_f/d_p}$$

where k_f is the thermal conductivity of the fluid.

2.6. Measurement uncertainty

An uncertainty analysis associated with the pressure drop and heat transfer measurements was performed by following the method detailed in Ref. [15]. For random error in pressure drop measurements, the static pressure change as a result of air density change due to temperature variations was small, since the range of operating temperature is small (typically less than 20 K). The uncertainty associated with the static pressure drop and the corresponding pressure loss coefficient was estimated to be less than 0.1% and 1.7%, respectively. The total uncertainty of the local heat transfer coefficient and Nusselt number was estimated to be 6.3% and 9.1%, respectively.

3. Numerical simulation

Steady state fluid-flow and heat transfer fields were obtained by solving the three-dimensional Reynolds Averaged Navier–Stokes (RANS) equations [16,17]. The standard k–ε turbulence model was used for turbulence closure. Apart from the entry and exit regions, the flow within the LFM has been experimentally observed to be periodic. This leads to the consideration of a unit cell. The unit cell used in the experiments was based on a structurally repeatable tetrahedral cell. A computational unit cell was chosen based on aerodynamic periodicity and symmetry of fluid flow within the LFM. At boundaries between the solid struts and flow domain, impermeable wall boundary conditions were imposed. Approximately 1.6×10^6 tetrahedral cells were distributed in the domain. The commercially available CFD code Fluent™ was used.

Flow across the computational unit cell of the LFM is assumed to be fully developed. This is reasonable for a unit cell placed apart from the entry and exit region. This enables a periodic boundary condition to be imposed at the inflow and outflow faces of the computational unit cell. The velocity profiles and magnitudes at inflow and outflow faces were set to be identical to conserve the mass flow rate crossing the faces. However, the pressure and temperature at these faces will be different. This is because pressure and temperature gradients exist in the flow direction. The shapes of the profiles are identical. It is only the mean level that changes. Fluent™ caters for this aspect of periodic flow. However, the use of periodic boundary conditions requires that the flow must be incompressible and the thermodynamic properties of the fluid such as heat capacity, thermal conductivity, viscosity and density, cannot be functions of temperature. All of the thermophysical properties were therefore determined at 298.15 K for the simulations.

For the fluid flow, either a pressure gradient ($\Delta P/L$) or a mass flow rate ($\dot{m}$) entering through the periodic face can be prescribed. In the current study, the mass flow rate was specified so that the pressure gradient ($\Delta P/L$) was to be obtained after the calculation. The pressure loss coefficient, K_{Cell} was calculated for each corresponding Reynolds number. The mean velocity can be obtained by integrating the flow velocities at the periodic surfaces.

For numerical accuracies, it was ensured that the calculated non-dimensional wall distance (y^+) was everywhere less than 8, where y^+ is defined as $y^+ = \rho u_\tau h_c/\mu$, u_τ is the friction velocity ($(\tau_w/\rho)^{1/2}$), τ_w is the wall shear stress, and h_c is the height of the first grid cell near the walls.

4. Fluid-flow and formation of vortex structures in a lattice-frame material

4.1. Overall flow pattern

In the present study, a single layer of the LFM was bounded between solid walls to form a sandwich heat exchanger. The fluid flow passes through the LFM between these walls, with the series of tetrahedral cells providing a tortuous flow passage. As shown in Fig. 1(b), the extent of the flow tortuousity depends on the orientation of the LFM. Two representative orientations were selected for the investigation: Orientation A for the most closed flow passage and Orientation B for the most open flow passage.

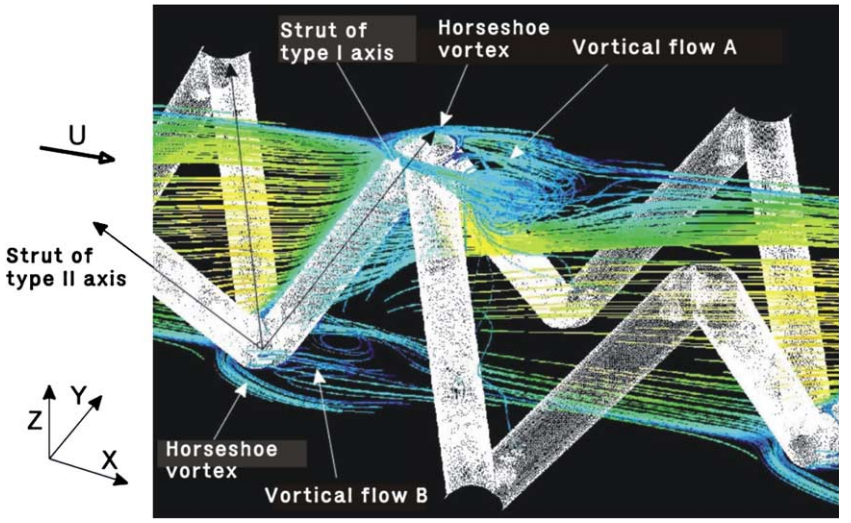

Fig. 6. Simulated local flow patterns over the LFM at $Re_{d_p} = 2.0 \times 10^4$ showing formation of vortex structures.

Prior to examining the detailed aspects of the fluid flow, it is instructive to examine the dominant flow structures in the LFM, which are believed to be responsible for the pressure loss and heat transfer. The fluid flow in Orientation A was calculated assuming a steady flow at $Re_{d_p} = 2.0 \times 10^4$. Fig. 6 shows the overall flow patterns, illustrated by pathlines originating from one of the symmetric faces and the bottom endwall. The flow past the LFM experiences stagnation and separation. The flow near the vertices where the struts meet the endwalls exhibits complex patterns. Vortex structures including 'horseshoe vortex' are clearly visible. The vortex flow pattern behind each vertex appears to be different from the horseshoe vortices.

The general flow patterns vary along the channel height due to the variation of spacing as a result of the inclined and yawed arrangements of the struts, leading to different flow features on the lower and upper endwall surfaces. Details of the local flow patterns around the LFM struts and on the endwall surfaces are discussed in the following sections.

4.2. Velocity distribution around the LFM struts

Given that the unit cell is chosen from the midsection of the LFM, it is reasonable to assume that the flow is fully developed. This implies that the incoming flow to the representative cell is already influenced by the upstream cells. Velocity contours at a plane in front of the strut of type I obtained from PIV measurements at $Re_{d_p} = 2.0 \times 10^4$ were used to compare with those calculated numerically. Fig. 4 illustrates the measurement planes (at $x = 0$) used for comparison, which coincides with the periodic face in the computational unit cell. It should be noted that the PIV technique only measures in-plane velocities, i.e., the y- and z-velocity components; the x-velocity component along the mainstream direction was not available.

Fig. 7(a) and (b) show contours of the y- and z-velocity components obtained from the CFD and the PIV. Overall, good agreement between measurement and prediction is observed. There are zero y-velocity lines along the centre of the strut of type I. These lines appear to indicate each side of the wake developed from the strut. It is seen from Fig. 7(b) that the flow behind the strut of type I is directed in the negative z direction (towards the lower endwall) whilst in the rest of the region, the flow is in the positive z direction (towards the upper endwall). This is associated with the topology of the strut of type I. The highest z-velocity occurs where the distance between the struts is the smallest (i.e. above vertex type 1). The negative velocity regions appear to be in the wake originated from the strut of type II.

4.3. Formation of vortex structures

The bounding of the LFM by the endwalls induces a strong secondary flow, which can be classified as two main types: (1) horseshoe type vortex in front of the LFM vertices and (2) secondary vortical flow motion behind the vertices. This section discusses these vortical motions and their mechanism of formation.

4.3.1. Horseshoe vortex

The existence of the struts/vertices causes the rolling up of the developed endwall boundary layer in front of the vertex of the LFM. In accordance with Kelvin's circulation theorem, the boundary layer vorticity cannot be

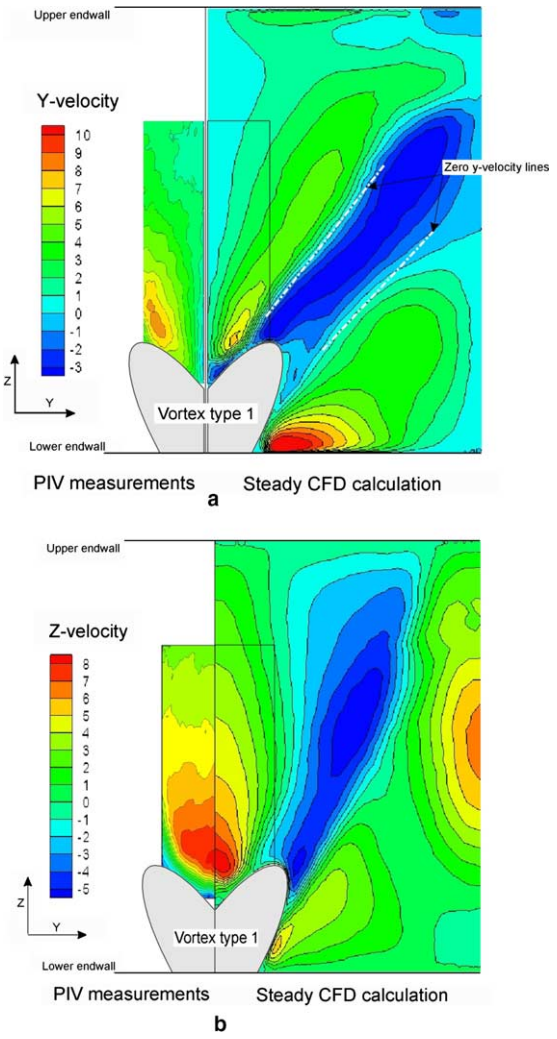

Fig. 7. Comparisons of the flow velocity fields at a plane obtained from the PIV measurements and steady CFD calculation at $Re_{d_p} = 2.0 \times 10^4$: (a) y-velocity component; (b) z-velocity component.

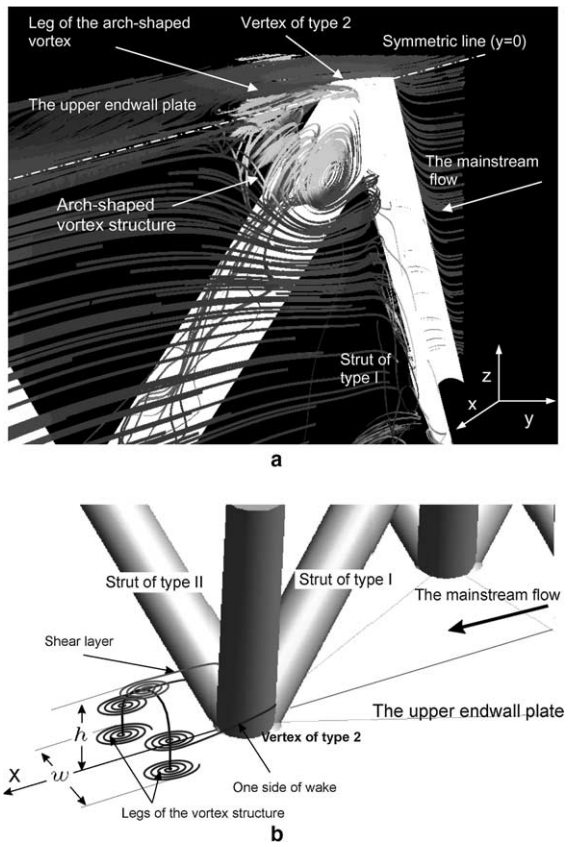

Fig. 8. An identified vortex structure (arch-shaped vortex) behind vertex of type 2: (a) calculated flow pattern at $Re_{d_p} = 2.0 \times 10^4$ where half of the arch-shaped vortex is shown; (b) sketch of formation of the arch-shaped vortex.

destroyed. Instead, it is convected around each side of the obstacle to form the two legs of the so-called "horseshoe" vortex. The high tangential velocity of the rolled up vorticity away from the core region interacts with the endwall surface, causing relatively high heat transfer.

More detailed flow patterns around the vertices are displayed in Fig. 6 at $Re_{d_p} = 2.0 \times 10^4$. Vortex structures including the horseshoe vortex were clearly observed at each vertex near the lower and the upper endwalls.

4.3.2. Arch-shaped vortex

The mechanism of formation of the vortical flow structures besides the horseshoe vortex, labelled as vortical flow 'A' and 'B' in Fig. 6, is discussed next. When the flow passes the vertex of type 2, the vortical flow pattern 'A' is formed. Fig. 8(a) displays the flow pattern behind the vertex, which was visualised by pathlines originating from the symmetric face. An arch-shaped vortex structure is clearly observed. This type of vortex pattern was addressed by Hussein and Martinuzzi [18]. They observed the arch-shaped vortex behind a cube mounted on a flat surface when the flow passes the cube. It was concluded that developed shear layers originating from three cube surfaces (two side surfaces and one top surface) were responsible for the arch-shaped vortex in the near wake.

The formation of the arch-shaped vortex in the LFM is associated with the topology of the LFM vertex. Fig. 8(b) illustrates a sketch of the formation of the arch-shaped vortex behind the vertex of type 2. One side of the wake developed from the strut of type II appears to form the legs of the vortex whilst the shear layer developed from the 'valley' made by the strut of type II, connects one pair of counterrotating vortices. The width of the vortex estimated to be $0.3S_y$ where S_y is a

transverse pitch of the LFM unit cell. The height of the vortex from the endwall surface was found to be $0.25(z/H)$ where H is the height of the LFM core.

The vortical flow pattern 'B' is formed behind the vertex of type 1. Fig. 9(a) shows pathlines released from the strut surfaces and the lower endwall, indicating a leg on the endwall and a half of the body of the vortex structure (only half of the flow domain is shown). However, the vortex pattern is somewhat different from that formed at the vertex of type 2. Its mechanism is schematically drawn in Fig. 9(b). Wakes developed from the vertex and the strut of type I appear to be responsible for this vortex structure. Both sides of the core line of extension of the concentrated vorticity regions (legs of the vortex) are inclined with respect to $y = 0$ plane. They meet at that plane, forming a vortex flow pattern as illustrated in Fig. 9(b). The width and height of the vortex formed at the lower endwall were estimated to be $0.3S_y$ and $0.25(z/H)$, respectively.

5. Local pressure distributions and overall pressure loss

5.1. Endwall flow patterns

In isotropic structures, the flow pattern is typically unidirectional. However, because of the structural anisotropy of the LFM, the flow patterns strongly depend on its orientation. In this section, endwall flow patterns corresponding to the two selected orientations, Orientation A and Orientation B, are considered. Again, the experimental measurements are compared to those predicted.

5.1.1. Orientation A

Fig. 10(a) and (b) show separately the flow patterns on the lower endwall obtained from the oil flow visualisation and the TLC measurements. Both were obtained from the smaller scale LFM model at $Re_{d_p} = 1.0 \times 10^4$ [9]. The entry effect in Orientation A disappears after

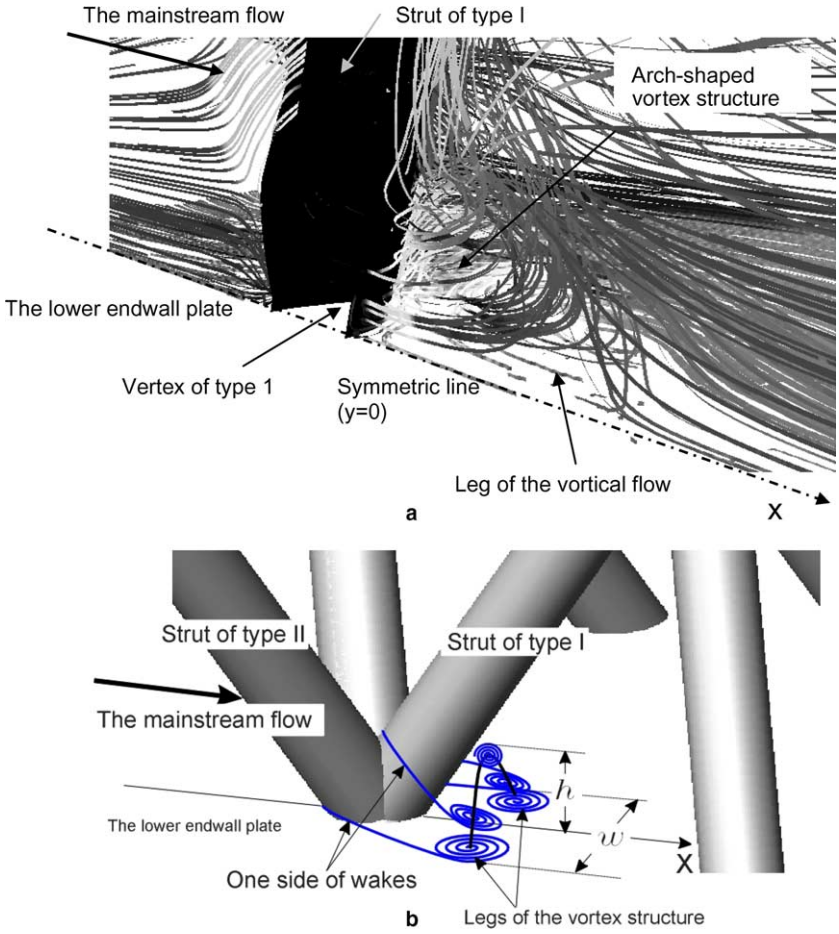

Fig. 9. An identified vortex structure (arch-shaped vortex) behind vertex of type 1: (a) calculated flow pattern at $Re_{d_p} = 2.0 \times 10^4$ where half of the arch-shaped vortex is shown; (b) sketch of formation of the arch-shaped vortex.

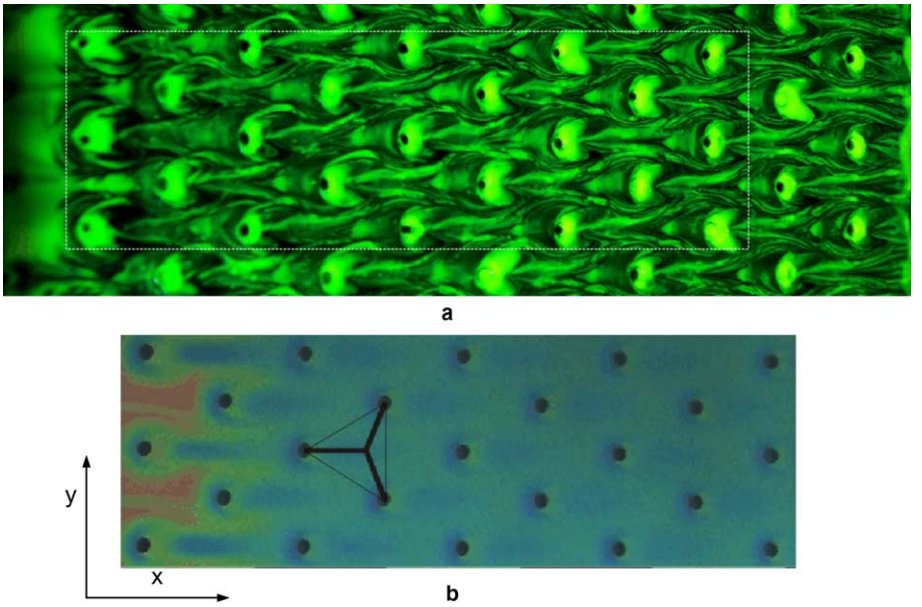

Fig. 10. Visualised endwall flow patterns for Orientation A obtained from: (a) oil flow visualization; (b) the TLC.

the second unit cell in the longitudinal direction (x-axis). In the rest of cells, very similar endwall flow patterns over each cell were observed. It also indicates that the flow is symmetric about a line of constant 'y' value through the centre of each vertex of the LFM.

The flow visualisation images show very low momentum regions on the downstream side of the vertices on the endwalls. The location of these appears to coincide with the position at which the legs of the arch-shaped vortices are located. Fig. 11(a) shows closed-up flow patterns of the two unit cells. This was obtained from the bigger LFM model used in this study by selecting one raw TLC image. More intensive flow interaction with the endwall was clearly observed in front of and behind the vertex. Fig. 11(b) presents the predicted flow pattern for Orientation A. There is a saddle point, which is singular point where zero shear stress exists, located in front of the stagnation point of the vertex. The regions (labelled as 'legs') where a concentrated vorticity associated with the arch-shaped vortices is situated correspond to the local minima of the endwall pressure distribution.

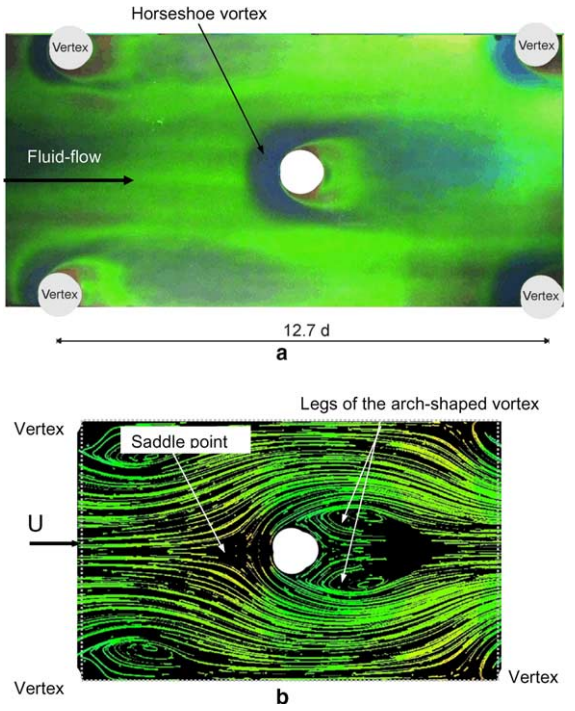

Fig. 11. Visualised endwall flow patterns for Orientation A obtained from: (a) TLC; (b) steady CFD calculation.

5.1.2. Orientation B

Orientation B is an orientation that is rotated 90° from Orientation A (see Fig. 1(b)). Fig. 12(a) and (b) show the endwall flow patterns obtained from the oil flow visualisation and the TLC measurements, respectively. In contrast to Orientation A, entry effects persist up to the fifth cell in Orientation B, highlighting a serpentine flow path caused at about 1/3 of the width of a unit cell. Furthermore, the axis of each horseshoe vortex is skewed with respect to x-axis at the centre of each vertex due to the structural asymmetry of the LFM struts.

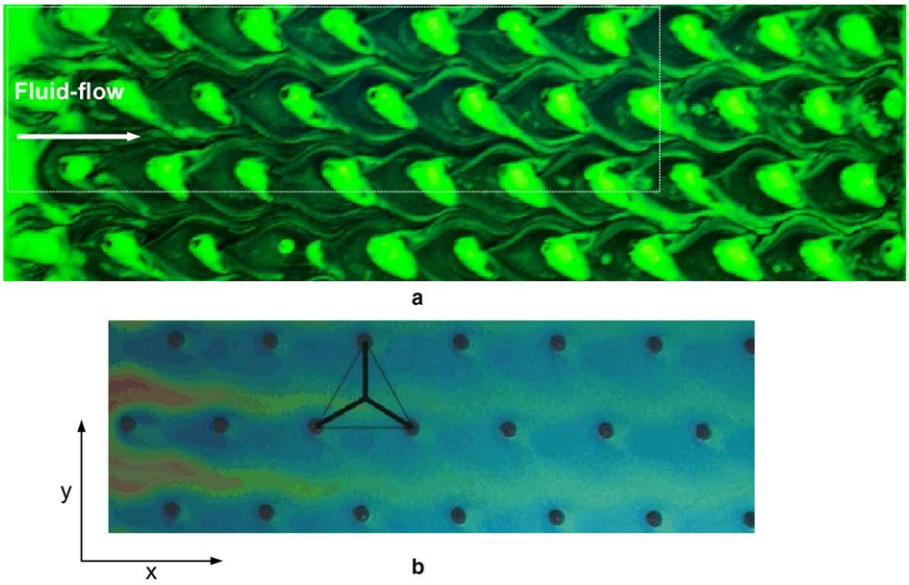

Fig. 12. Visualised endwall flow patterns for Orientation B obtained from: (a) oil flow visualization; (b) TLC.

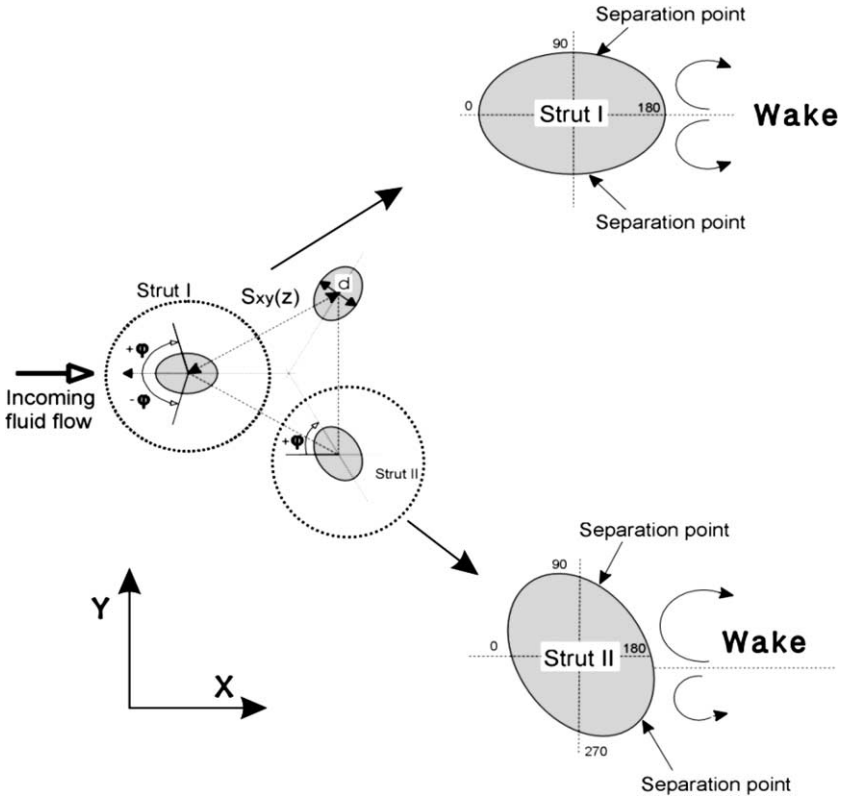

Fig. 13. Configuration of a unit cell in Orientation A, showing two different types of struts.

The endwall flow images of the two orientations have common features such as the formation of the horseshoe vortex at each vertex, the lower momentum regions at the downstream side of the vertices and relatively high flow interaction regions behind the vertices. However, the mainstream flow patterns in each unit cell and

around each vertex of both orientations are generally different.

5.2. Flow pattern and pressure distribution on strut surfaces: Orientation A

The focus of detailed flow patterns and pressure distribution on the strut surface was placed on Orientation A. The unit cell of the LFM consists of one strut of type I and two struts of type II as illustrated in Fig. 13. The surface flow pattern and the corresponding pressure distribution are considered separately for each strut type in this section.

5.2.1. Strut of type I

The strut of type I is inclined at (+)35.17° to a plane normal to the mainstream flow direction where a positive (+) signed angle denotes the angle rotated to the downstream direction from the axis normal to the flow direction. The flow around this strut is expected to be symmetric with respect to the strut axis (z'-axis).

To observe the flow pattern on the strut surface, a flow visualisation was performed at $Re_{d_p} = 1.0 \times 10^5$ using the oil–dye mixture technique. The result is displayed in Fig. 14(a), showing the variation of the flow separation point with the spanwise strut length (z'-axis). Two distinct regions were identified based on the location of the separation line: Region 1: $0.1 < z/H < 0.27$ and Region 2: $0.27 < z/H < 0.8$ where z/H is the height-wise location normalized by the channel height (H). Correspondingly, the locations of the flow separation φ satisfy: (1) $0° < \varphi < 80°$ and (2) $80° < \varphi < 100°$, where φ is an azimuth angle. As z/H increases (i.e. moving away from the connected upstream struts of type II), the separation line moves downstream until above $z/H = 0.27$ where the separation line does not appear to be affected by the upstream struts of type II, yielding a line parallel to the strut axis.

In conjunction with the oil flow visualisation, the static pressure distribution on the strut surface was measured at $Re_{d_p} = 2.0 \times 10^4$. A total of 360 pressure data points from 24 azimuth angles and 15 spanwise locations were used for the contour plot where the 0° azimuth angle points coincide with the stagnation points. The results are shown in Fig. 14(b).

Of interest are the low pressure regions labelled 'A' and 'B' in Fig. 14(b). Region 'A' is located at the spanwise location of $z/H \sim 0.3$ and at $\varphi = 60°$. The low pressure spots result from a high velocity flow. To examine this, particles were "released" in the CFD from the symmetric face to form pathlines, highlighting this region. Fig. 15 illustrates the formation of a vortical flow pattern near the stagnation point at $z/H = 0.3$. After the flow stagnates, the spanwise velocity component ($-z'$-velocity, toward the lower endwall) forms the vortex. This vortex is then convected downstream by the

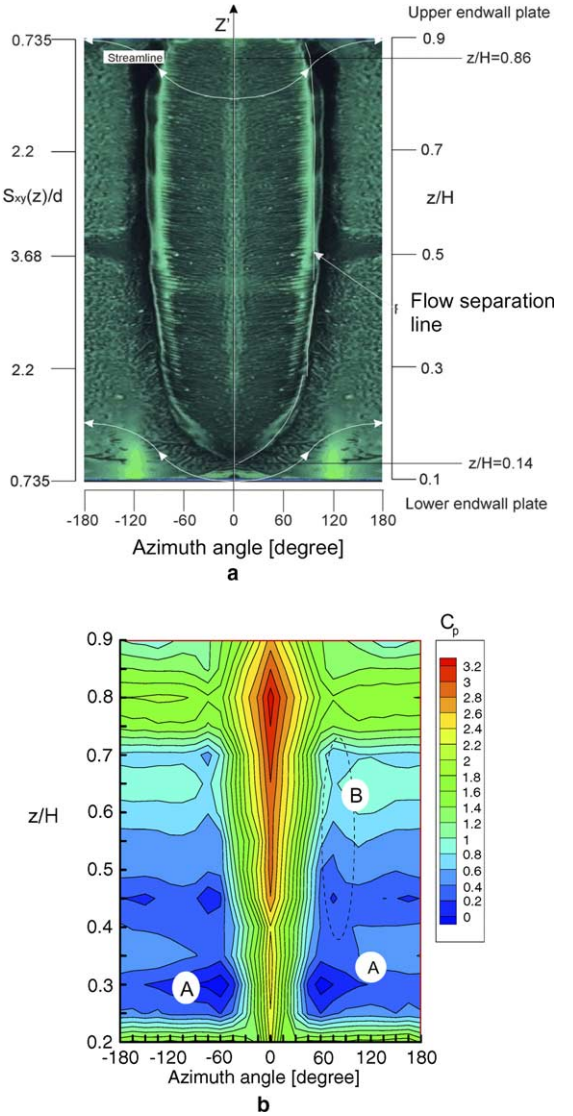

Fig. 14. Flow on strut surface of type I, (a) surface flow pattern obtained using oil flow visualization technique at $Re_{d_p} = 1.0 \times 10^5$; (b) static pressure distribution on strut of type I at $Re_{d_p} = 2.0 \times 10^4$.

mainstream flow. A high angular velocity component of the vortical flow interacts with the strut surface near $z/H = 0.3$ resulting in the low pressure regions. Another low pressure region labelled as 'B' ranges from $z/H = 0.45$ to 0.7 along the spanwise location. There is relatively high velocity near the mid-height region, e.g., $0.3 < z/H < 0.7$. As this higher, than that near both endwalls, velocity flow convects over the struts, it causes greater changes in static pressure due to its higher dynamic pressure, resulting in the lower surface pressure in the region 'B'.

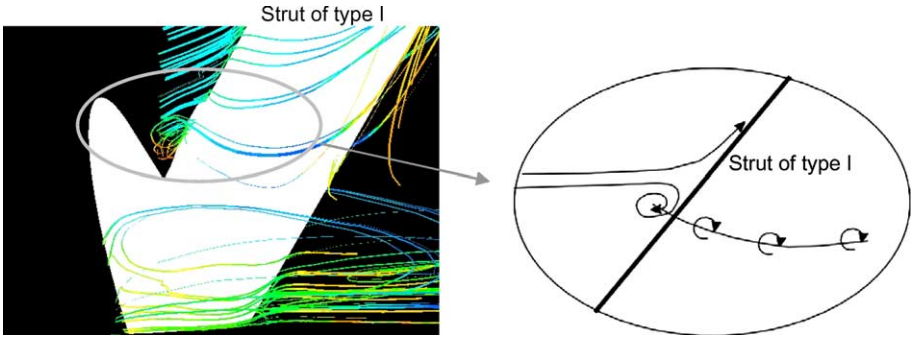

Fig. 15. Simulated flow feature at $z/H \sim 0.3$ showing formation of a vortical flow on strut of type I at $Re_{d_p} = 2.0 \times 10^4$.

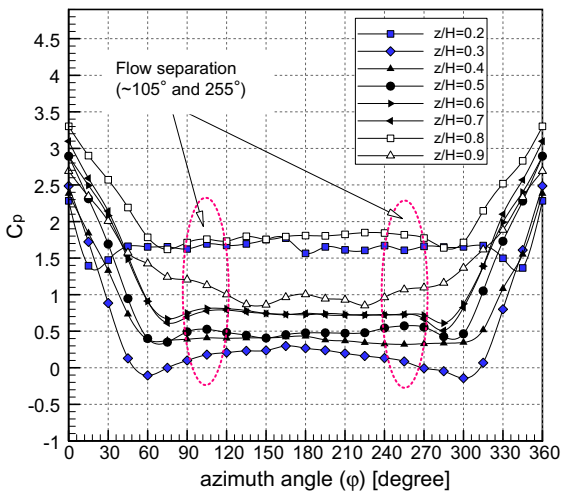

Fig. 16. Variation of C_p along circumference of strut of type I at $Re_{d_p} = 2.0 \times 10^4$.

In order to evaluate the location of the flow separation along the circumference of the strut, the measured static pressure data were replotted in Fig. 16. The results indicate that flow separation occurs around $\varphi \sim 105°$. However, the flow separation near each end of the strut (i.e. $z/H = 0.2$, and 0.9) takes place at different azimuth angles. For example, at $z/H = 0.2$ near the vertex of type 1, the separation point is about 45°. For $z/H = 0.9$ near the vertex of type 2, it is difficult to determine the separation point. It should be noted that the location of the flow separation obtained from the flow visualisation and the static pressure distribution is slightly different. This is due to the use of the oil on the strut surface for the visualisation, which changes the flow patterns due to the viscosity of the oil.

5.2.2. Strut of type II

A strut of type II is inclined at $\sim(-)22°$ in the x–z plane measuring from the z-axis and yawed at $\sim(\pm)31°$ in the x–y plane measuring from x-axis, respectively.

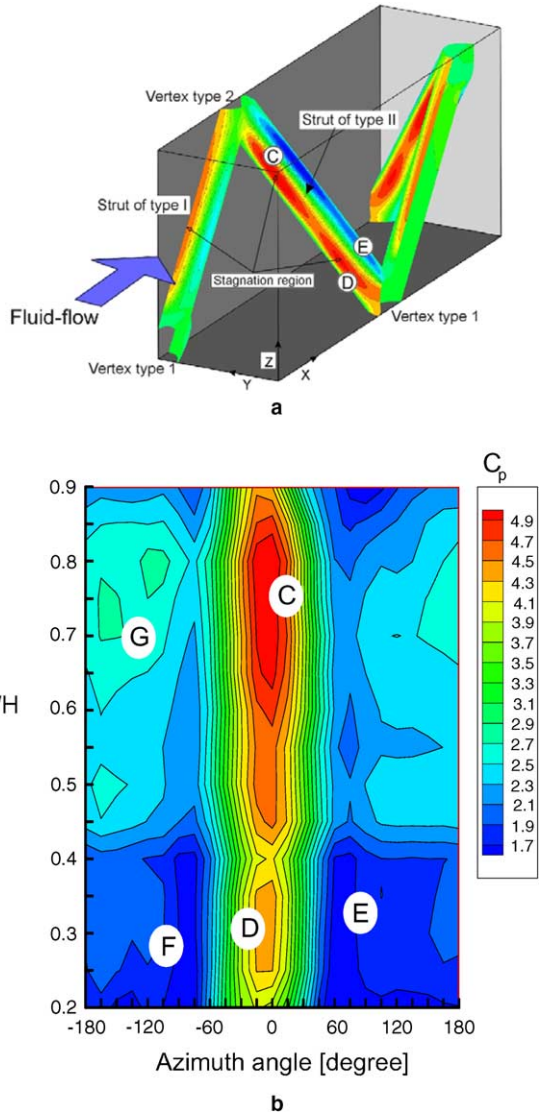

Fig. 17. Static pressure distribution on strut of type II at $Re_{d_p} = 2.0 \times 10^4$: (a) pressure distribution on each strut from the CFD simulation; (b) measured C_p contour.

Fig. 17(a) illustrates the configuration of the unit cell including the strut of type II; it also shows the predicted static pressure distribution on the struts. Fig. 17(b) displays the experimentally measured static pressure contour on the strut surface. Five distinct pressure regions were observed labelled as 'C', 'D', 'E', 'F' and 'G'. The regions 'C' and 'D' coincide with the flow stagnation on the strut. Region 'F' has similar features as region 'E'.

Region 'G' is located near the vertex of type 2 (at the upper endwall) whereas 'E' and 'F' are near the vertex type of 1 (at the lower endwall). In regions 'E' and 'G', the flow experiences acceleration due to the blockage caused by the struts. This high momentum flow interacts with the strut surface causing a low surface pressure. It is thought that the formation of horseshoe vortex originating at the vertices of types 1 and 2 is responsible for the other lower pressure region, 'F'. Here, a high angular velocity of the horseshoe vortices generates the low surface pressure.

The measured pressure data were replotted in Fig. 18 to evaluate the flow separation points along the span in comparison with Fig. 16 for the strut of type I, the variation of the pressure distribution at different spanwise locations is not as pronounced. Peak values of the base pressure are located at approximately $\varphi = 195°$. The circumferential variation of the static pressure is asymmetric, with lower pressure at the inside of the strut than that at the outside. The flow blockage generated by the struts accelerating the flow past these regions causes the low surface pressure on the strut.

5.3. Overall pressure loss

The variation of the overall pressure loss over a wide range of Reynolds numbers was studied experimentally

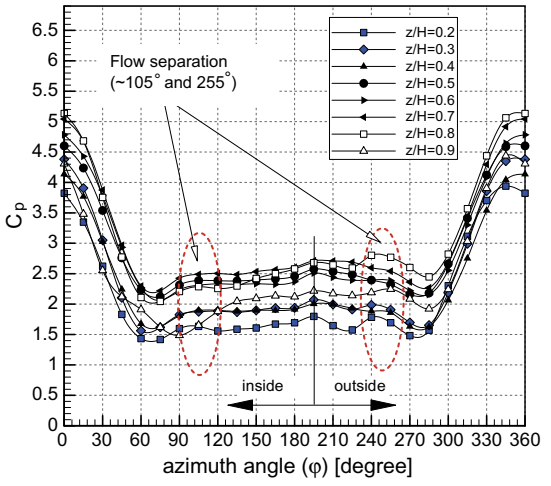

Fig. 18. Variation of static pressure along circumference of strut of type II at $Re_{d_p} = 2.0 \times 10^4$.

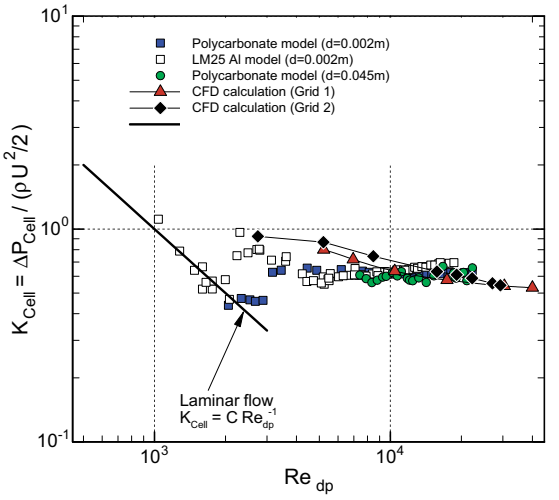

Fig. 19. Comparisons of the pressure loss coefficients obtained from the measurements and the CFD simulation.

and numerically; the results are shown in Fig. 19. It can be seen that the flow is laminar when $Re_{d_p} < 2000$, with the pressure drop decreasing as the Reynolds number is increased. In this regime, the viscous effect dominates since $K_{\text{Cell}} \sim CRe_{d_p}^{-1}$ where $C \approx 1000$.

The transition from laminar to form-dominated flow occurs in the range of $2000 < Re_{d_p} < 3000$. The pressure loss coefficient of all models approaches asymptotic values after the transition if the Reynolds number is larger than 4500. This means that the pressure drop (ΔP) across the unit cell is proportional to square of the flow velocity (U) since K_{Cell} is approximately constant. As the flow is in high Reynolds number regime, i.e., $Re_{d_p} > 4500$, the pressure loss becomes independent of the skin friction (viscous drag) due to the predominance of form drag in the total drag [19,20].

The simulated results of the pressure loss coefficient from two different mesh densities are included in Fig. 19. Grid 1 denotes a course mesh with 0.6 million tetrahedral cells and Grid 2 is a more refined mesh with 1.6 million cells. Given the complexity of the LFM structure and the large computational size, the agreement between prediction and measurement is fairly good. It is believed that the slightly underestimation of the pressure losses when $Re_{d_p} > 2.0 \times 10^4$ is due to the delay in flow separation in the CFD simulation, causing a reduction of the form drag.

To confirm this, comparisons of the C_p data of the measurements with that of the CFD were made for a selected spanwise location at $z/H = 0.5$ for both types of struts where H is the unit cell height (see Fig. 20). For the strut of type II, the flow separation was numerically predicted to occur at $\varphi = 120°$ (inside) and $\varphi = 240°$ (outside), compared to the measured angles of $\varphi = 105°$

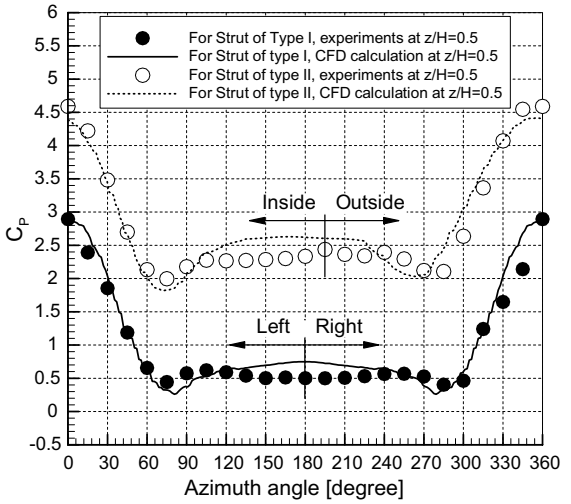

Fig. 20. Comparisons of circumferential variation of C_p obtained from the experiments and the CFD calculation for midspan of the struts at $Re_{d_p} = 2.0 \times 10^4$.

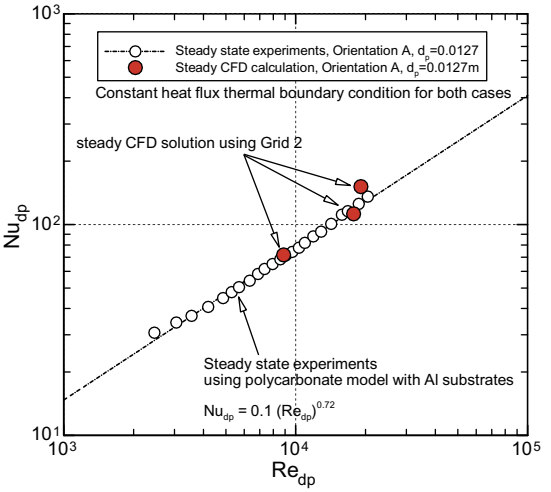

Fig. 21. Comparison of average Nusselt numbers obtained from measurements and CFD simulation for Orientation A.

(inside) and $\varphi = 255°$ (outside). On the other hand, the flow around the strut of type I is symmetric and the flow separation was taken place at $\varphi = 135°$ (and $\varphi = 225°$) from the CFD compared to the measured angle of $\varphi = 105°$.

6. Overall heat transfer characteristics and local heat transfer distribution

6.1. Overall heat transfer behaviour

Of particular interest is the amount of heat which can be removed by the LFM for a given porosity and solid conductivity. In order to evaluate overall heat transfer performance, experiments were conducted using the LFM model made from polycarbonate, having the porosity of 0.938. Details associated with the experiments can be found in [7–9] where data obtained from small LFM models made with aluminium alloy were also reported.

The overall heat transfer behaviour of the polycarbonate LFM model with aluminium substrates (endwalls) is plotted against Reynolds number in Fig. 21. Forced convection along Orientation A with constant wall heat flux was used. The results are empirically correlated as a function of Reynolds number as

$$Nu_{d_p} = 0.14(Re_{d_p})^{0.68}$$

Fig. 21 also includes results obtained from CFD calculations, and very good agreement with experiments is observed.

6.2. Effect of the vortex structures in local endwall heat transfer

A further examination of the local heat transfer patterns is necessary to understand the detailed heat transfer mechanisms. To narrow the focus, Orientation A was selected due to its complexity of the fluid flow and the heat transfer patterns. In previous sections, it was shown that the high surface heat transfer occurred in front of the vertices. This is due to the formation of the horseshoe vortex. Besides this region, another high heat transfer area exists behind the arch-shaped vortex structures.

The heat transfer map of the lower endwall surface is given in Fig. 22(a) obtained from the TLC measurements at $Re_{d_p} = 2.0 \times 10^4$. An additional map shown in Fig. 22(b) was obtained from the CFD simulation, with the constant wall heat flux boundary condition imposed at the same Reynolds number. In general, there is good agreement between CFD simulation and experimental measurements. The CFD captures all of the local features including the formation of the horseshoe and arch-shaped vortices.

To examine the influence of vortex structures on the surface heat transfer, a further comparison was made in Fig. 23 for two different axial locations along the flow direction. It is seen that four distinct heat transfer regions exist, described as follows:

Region (1): region under influence of horseshoe vortex ($180 < Nu_{d_p} < 250$),
Region (2): region under influence of arch-shaped vortex and recirculating flow ($165 < Nu_{d_p} < 180$),

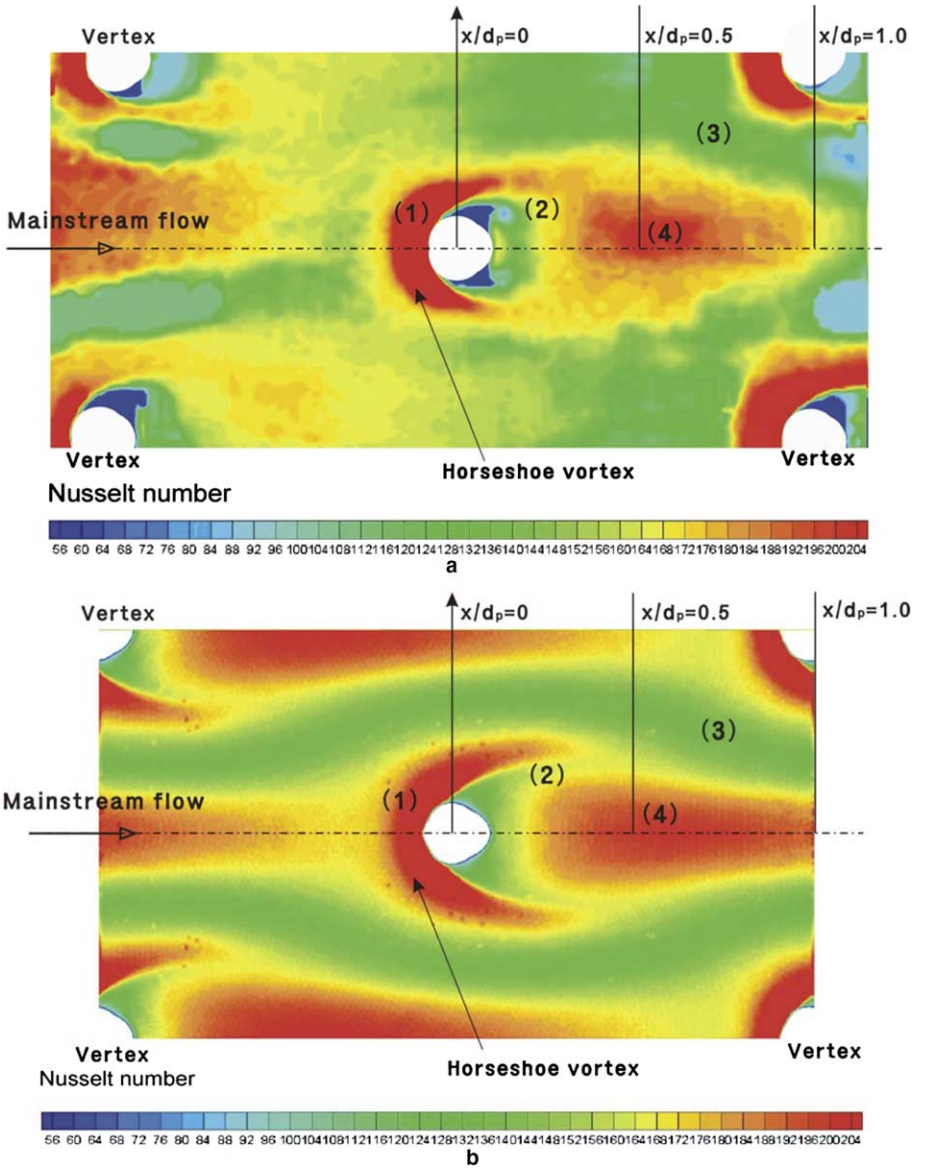

Fig. 22. Comparisons of the surface Nusselt number distributions of lower endwall plate in Orientation A at $Re_{d_p} = 2.0 \times 10^4$ contained from: (a) TLC; (b) CFD simulation.

Region (3): free flow passage ($110 < Nu_{d_p} < 165$), and
Region (4): region under influence of reattached flow ($Nu_{d_p} > 200$).

As distinguished from the horseshoe vortex, the arch-shaped vortex and recirculated flow also cause the higher heat transfer behind the vertex than that in the free flow passage. The CFD gives an underprediction of approximately 25% in regions under the influence of these vortex flows, whilst a good prediction for the free flow passage was observed. It could be said that the presence of the vortex flows increases the local surface heat transfer by about 180% compared with that in the free flow passage.

In summary, the formation of the vortex structures increases the local endwall heat transfer by means of promoting the flow mixing around the vertices. This feature is repeated at each vertex. Although the spacing ratio between the vertices is large ($S_{xy}/d = 7.35$), the staggered manner of the LFM vertices and wakes originating from the struts appears to contribute to the increase in endwall heat transfer.

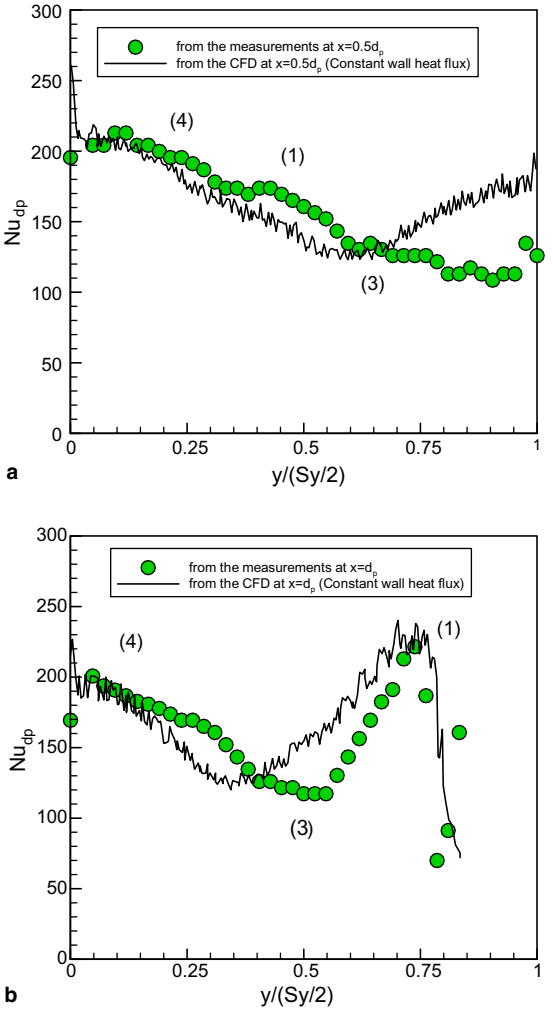

Fig. 23. Comparisons of local surface Nusselt numbers measured using the TLC with those from the CFD calculation at $Re_{d_p} = 2.0 \times 10^4$ for selected longitudinal location on the lower endwall: (a) at $x/d_p = 0.5$; (b) at $x/d_p = 1.0$.

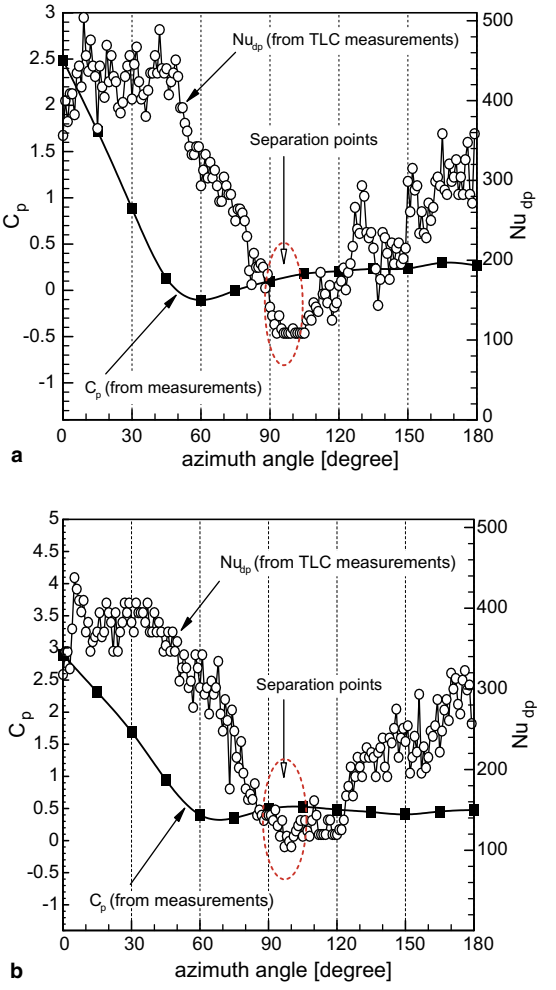

Fig. 24. Comparison of circumferential variation of the Nusselt number on the strut of type I obtained from the TLC at $Re_{d_p} = 2.0 \times 10^4$: (a) at $z'/l = 0.3$ and (b) at $z'/l = 0.5$.

6.3. Detailed surface heat transfer on the strut of type I

The circumferential distributions of the Nusselt number were measured at selected spans of the strut of type I. The locations were $z'/l = 0.3$ and 0.5 where z' is the strut axis and l is the strut length. The distributions were obtained using the TLC technique at $Re_{d_p} = 2.0 \times 10^4$ with the azimuth angle measured from the stagnation point.

In Fig. 24(a), the circumferential variation of the static pressure coefficient (C_p) is plotted together with that of Nusselt number for $z'/l = 0.3$. From the C_p variation curve, it seems that the flow separation occurs at around $\varphi = 105°$. The Nu_{d_p} variation around the strut circumference shows a very similar flow separation point. In general, moving away from the stagnation point, the heat transfer decreases until the flow separates at which point the heat transfer is at its lowest.

Fig. 24(b) displays the Nusselt number variation at $z'/l = 0.5$ where the least interference from neighbouring struts is expected. A very similar heat transfer pattern along the azimuth angle to that at $z'/l = 0.3$ was observed. About 15% less heat transfer in the stagnation region was achieved compared to that at $z'/l = 0.3$.

6.4. Contribution of local flow features to the overall heat transfer

The local heat transfer associated with the various flow features has been identified through the previous sections. For the LFM of porosity of 0.938, the endwalls and struts occupy 60% and 40% of the total surface area

in the LFM as displayed in Fig. 25(a). The vortex structures dominate the heat transfer on the endwalls. The strut surface heat transfer pattern shows distinguished patterns before and after the flow separation. This section, in turn, attempts to integrate these local heat transfer patterns to examine their contribution to the total heat transfer performance.

The circumferential variation of the heat transfer on the strut surface is distinguished before and after the flow separation. Since this occurred typically at 105° for the strut of type I (from the experiments), the Nusselt numbers over regions from the stagnation line ($\varphi = 0°$) to the separation point ($\varphi = 105°$) were spatially averaged, as

$$Nu_{d_p} = \frac{1}{\varphi_2 - \varphi_1} \int_{\varphi_1=0°}^{\varphi_2=105°} Nu_{d_p}(\varphi)\,\Delta\varphi$$

(before flow separation)

$$Nu_{d_p} = \frac{1}{\varphi_2 - \varphi_1} \int_{\varphi_1=105°}^{\varphi_2=180°} Nu_{d_p}(\varphi)\,\Delta\varphi$$

(after flow separation)

where $Nu_{d_p}(\varphi)$ is the measured Nusselt number at each azimuth angle. Similarly, for the strut of type II, the averaged Nusselt number before the flow separation is

$$Nu_{d_p} = \frac{1}{\varphi_2 - \varphi_1} \int_{\varphi_1=0°}^{\varphi_2=105°} Nu_{d_p}(\varphi)\,\Delta\varphi \quad \text{and}$$

$$Nu_{d_p} = \frac{1}{\varphi_2 - \varphi_1} \int_{\varphi_1=255°}^{\varphi_2=360°} Nu_{d_p}(\varphi)\,\Delta\varphi$$

and, after the flow separation, it is

$$Nu_{d_p} = \frac{1}{\varphi_2 - \varphi_1} \int_{\varphi_1=105°}^{\varphi_2=255°} Nu_{d_p}(\varphi)\,\Delta\varphi$$

Using these formulas, it has been established that the regions before and after the flow separation contribute 65% and 35% to the average strut heat transfer, respectively, as shown in the pie chart in Fig. 25(b).

As discussed in Section 6.2, the formation of the horseshoe vortex and arch-shaped vortex structures cause an increase in the local heat transfer by up to

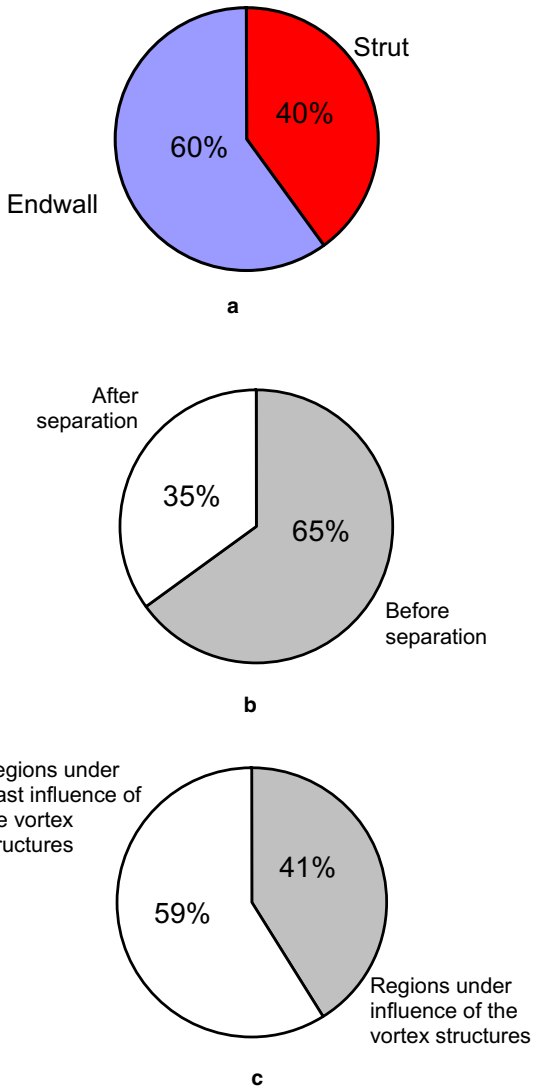

Fig. 25. Estimation of the contribution of the endwall and strut surfaces to the overall heat transfer for $\varepsilon = 0.938$ at $Re_{d_p} = 2.0 \times 10^4$: (a) surface area density fraction; (b) effect of the flow separation on the heat transfer from the strut surface; (c) contribution of the vortex structures.

Table 2
Estimated contribution of the local flow features

		Fraction of total area (%)	Area-averaged Nu_{d_p} (measured)	Fraction of average Nu_{d_p} (%)	Total area-averaged Nu_{d_p}	Fraction of total Nu_{d_p} (%)
Strut	Before separation	23.2	292.7	37	260 (of struts)	57
	After separation	16.8	214.7	20		
Endwall	Under influence of vortex structures	22.2	181.4	18	163 (of endwall)	43
	Under least influence of vortex structures	37.8	152.2	25		

All of the data were measured from TLC at $Re_{d_p} = 2.0 \times 10^4$ for both the endwall and the struts.

180%. Four distinct regions were identified, based on the local Nusselt number values, which correspond to the local flow features. From the measurements using the TLC, the surface area-averaged Nusselt number was obtained using:

$$Nu_{d_p}(\text{Endwall}) = \frac{1}{A_{\text{endwall}}} \int Nu_{d_p}(x,y)\,\Delta x\,\Delta y \qquad (3)$$

where A_{endwall} is the area of the endwalls, $Nu_{d_p}(x,y)$ is the measured local Nusselt number on the endwall surface. The formation of the vortex structures contributes up to 41% of the total endwall heat transfer as shown in Fig. 25(c). Contributions of the aforementioned local heat transfer patterns to the overall heat transfer of the LFM were calculated as

$$\frac{Nu_{d_p}(\text{Endwall})A_{\text{endwall}}}{(Nu_{d_p})_{\text{total}}A_{\text{total}}} \quad (\text{Endwalls})$$

$$\frac{Nu_{d_p}(\text{Strut})A_{\text{strut}}}{(Nu_{d_p})_{\text{total}}A_{\text{total}}} \quad (\text{Struts})$$

where $(Nu_{d_p})_{\text{total}}$ represents the total heat transfer in the LFM including the endwall and strut surfaces and A_{strut} is the area of strut surfaces. Details are listed in Table 2.

A detailed breakdown of the local heat transfer on the endwall and strut surfaces of the LFM subjected to forced convection along Orientation A is shown in Fig. 26. It can be summarised as follows:

(1) the strut region before the flow separation causes 37% of the total heat transfer;
(2) the strut region after the flow separation contributes 20% of the total heat transfer;
(3) the region on the endwall on which the vortex structures affect causes 18% of the total heat transfer;
(4) the region on endwall on which the vortex structures reach least effect contributes 25% of the total heat transfer.

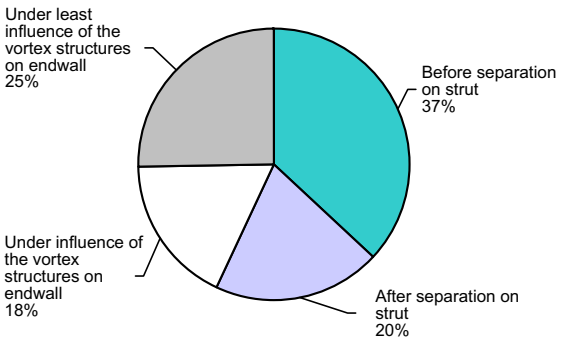

Fig. 26. Contribution of significant flow features to the overall heat transfer at $Re_{d_p} = 2.0 \times 10^4$.

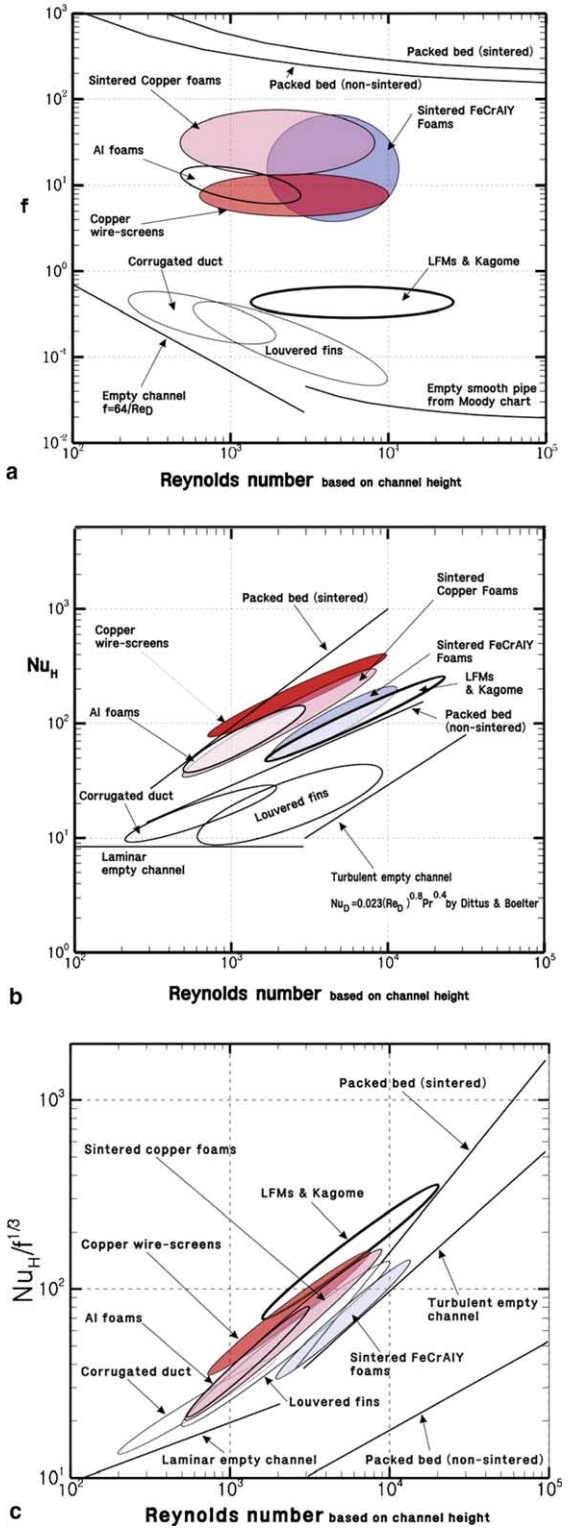

Fig. 27. Performance charts of different heat dissipation media: (a) friction factor; (b) heat transfer; (c) efficiency index $Nu_H/f^{1/3}$.

7. Comparison with other porous heat dissipation media

The thermohydraulic performance of the LFMs (aluminium alloy) is compared with the following types of porous heat dissipation medium: brazed copper textiles [21], Kagome structures (bronze) [22], metal foams (copper and FeCrAlY—a steel alloy) fabricated with the relatively cheap sintering [23,24], aluminium foams made with the expensive investment casting [25], packed beds with non-sintered steel beads and with sintered bronze beads [26], aluminium louver fin arrays [27], and corrugated ducts with sinusoidal wavy passage [28]; empty channel [29] is also included as datum. The LFMs and Kagome structures are both periodic lattice materials and highly porous ($\varepsilon \sim 0.9$), consisting a 3D network of cylindrical trusses. The porosity of the packed beds, about 0.4, is much smaller than that of the metal foams (about 0.9).

For consistence with the published data of the selected media, the channel height is used as the length scale of the friction factor f, Nusselt number Nu_H and Reynolds number Re_H. The results are plotted in Fig. 27(a) and (b). Furthermore, the thermal efficiency index ($Nu_H/f^{1/3}$) for each selected medium is plotted as a function of Re_H in Fig. 27(c). Physically, the chart of Fig. 27(c) ranks the heat transfer capabilities of different heat dissipation media at a *fixed* pumping power. Fig. 27(c) reveals that all the heat dissipation media considered in this paper are better heat exchangers than an empty channel, except for the packed bed with non-sintered metallic particles. Note also that, in the form-dominated regime ($Re_H > 1000$), periodic materials (LFMs, Kagome structures and copper textiles) have superior thermal efficiency to other media, and their overall performance may be further enhanced by optimizing the topology and porosity.

8. Conclusion

The local dominant flow features in the single layered LFM sandwich heat exchanger that consists of the tetrahedral unit cells were identified. These are the vortex structures formed behind the vertices of the LFM and the flow separation on the strut surfaces. The vortex structures include the horseshoe vortices formed in front of the vertices and the arch-shaped vortices behind the vertices.

It was found that the horseshoe vortex increases local heat transfer of the endwall regions up to 180% more than that of regions where the least influence of the horseshoe vortex is present. The arch-shaped vortex forms the regions of flow recirculation and reattachment, leading to relatively high heat transfer. The location of flow separation along the strut varies with spanwise position due to presence of the vertices (or endwalls). The regions on the strut surface before the flow separation contributed approximately 40% of the total heat transfer in the LFM. It implies that the delay of the flow separation may lead to an increase in the overall heat transfer.

Performance charts are presented to compare aluminium LFMs with selected heat dissipation media including metal foams, Kagome structures, brazed copper textiles, packed beds, corrugated ducts, and louvered fins. Significant opportunities exist to maximise the heat transfer performance of periodic cellular metals varying the pore fraction, anisotropy of the pores and metallic alloy used. For multifunctional applications further optimisation requires simultaneous consideration of their thermal and structural properties.

Acknowledgements

This work was supported by the UK Engineering and Physical Sciences Research Council (EPSRC Grant No. EJA/U83) and the US Office of Naval Research (ONR Grant No. N000140110271). T.J. Lu also wishes to thank the support from the National Science Foundation of China (Grant No. 10328203). T. Kim is grateful to Brain Korea 21 project 2004–2005 for the financial support during the preparation of this manuscript.

References

[1] A.G. Evans, J.W. Hutchinson, M.F. Ashby, Multifunctionality of cellular metal systems, Prog. Mater. Sci. 43 (1999) 171–221.
[2] S. Chiras, D.R. Mumm, A.G. Evans, N. Wicks, J.W. Hutchinson, K. Dharmasena, H.N.G. Wadley, S. Fichter, The structural performance of near-optimized truss core panels, Int. J. Solid Struct. 39 (2002) 4093–4115.
[3] N. Wicks, J.W. Hutchinson, Optimal truss plates, Int. J. Solid Struct. 38 (2001) 5165–5183.
[4] J.C. Wallach, L.J. Gibson, Mechanical behaviour of a three-dimensional truss material, Int. J. Solid Struct. 38 (2001) 7181–7196.
[5] V.S. Deshpande, N.A. Fleck, M.F. Ashby, Effective properties of the octet-truss lattice material, J. Mech. Phys. Solid 49 (2001) 1747–1769.
[6] V.S. Deshpande, N.A. Fleck, Collapse of truss core sandwich beams in 3-point bending, Int. J. Solid Struct. 38 (2001) 6275–6305.
[7] T. Kim, C.Y. Zhao, H.P. Hodson, T.J. Lu, Convective heat dissipation with lattice-frame materials, Mech. Mater. 36 (2004) 767–780.
[8] T. Kim, Fluid-flow and heat transfer in a lattice-frame material, Ph.D. Thesis, Department of Engineering, University of Cambridge, UK, 2004.
[9] T. Kim, H.P. Hodson, T.J. Lu, Fluid-flow and endwall heat-transfer in untralightweight lattice-frame materials, Int. J. Heat Mass Transfer 47 (2004) 1129–1140.
[10] T. Kim, H.P. Hodson, T.J. Lu, Pressure loss and heat transfer mechanisms in a lattice-frame structured heat

exchanger, J. Mech. Eng. Sci., IMechE Proceeding, in press.
[11] Z. Wang, D.R.H. Gillespie, P.T. Ireland, Advances in heat transfer measurements using liquid crystals, Turbulent Heat Transfer (Engineering Foundation) San Diego, CA, 1996, pp. 1–25.
[12] D.R.H. Gillespie, Z. Wang, P.T. Ireland, S.T. Kohler, Full surface local heat transfer coefficient measurements in a model of an integrally cast impingement cooling geometry, ASME J. Heat Transfer V120 (1998) 92–99.
[13] D.R.H. Gillespie, Intricate internal cooling system for gas turbine blading, D. Phil Thesis, Department of Engineering Science, University of Oxford, UK, 1996.
[14] D.A. Nield, A. Bejan, Convection in Porous Media, second ed., Springer, Berlin, 1998.
[15] H.W. Coleman, W.G. Steele, Experimentation and Uncertainty Analysis for Engineers, second ed., Wiley Inter-Science, 1999.
[16] FLUENT 5/6, User's Guide, Fluent Inc., Lebanon, NH 1-4, USA, 1998.
[17] GAMBIT 2.0, User's Guide, Fluent Inc., Lebanon, NH 1-4, USA, 1998.
[18] H.J. Hussein, R.J. Martinuzzi, Energy balance for the turbulent flow around a surface mounted cube placed in a channel, Phys. Fluids 8 (1996) 764–780.
[19] M.M. Zdravkovich, Flow around circular cylinders, Applications, vol. 1, Oxford Science Publications, 1997.
[20] M.M. Zdravkovich, Flow around circular cylinders, Applications, vol. 2, Oxford Science Publications, 2003.
[21] J. Tian, T. Kim, T.J. Lu, H.P. Hodson, D.J. Sypeck, H.N.G. Wadley, the effect of topology upon fluid-flow and heat-transfer within cellular copper structures, Int. J. Heat Mass Transfer 47 (2004) 3171–3186.
[22] F. Hoffmann, T.J. Lu, H.P. Hodson, Heat transfer performance of Kagome structures, in: Proc. 8th UK National Heat Transfer Conference, Oxford, 9–11 September 2003.
[23] C.Y. Zhao, Thermal transport in cellular metal foams with open cells, Ph.D. Thesis, Department of Engineering, University of Cambridge, 2003.
[24] C.Y. Zhao, T. Kim, T.J. Lu, H.P. Hodson, Thermal transport in high porosity cellular metal foams, AIAA, J. Thermophys. Heat Transfer 18 (3) (2004) 309–317.
[25] S.Y. Kim, B.H. Kang, J.H. Kim, Forced convection from aluminium foams in an asymmetrically heated channel, Int. J. Heat Mass Transfer 44 (2001) 1451–1454.
[26] P.X. Jiang, M. Li, T.J. Lu, Z. Ren, X. Sun, Convection heat transfer in sintered porous plate channels, in: Proc. 12th International Conference on heat Transfer, Grenoble, France, August 2002.
[27] W.M. Kays, A.L. London, Compact heat exchangers, third ed., McGraw-Hill, 1984.
[28] H. Blomerius, C. Holsken, N.K. Mitra, Numerical investigation of flow field and heat transfer in cross corrugated ducts, ASME J. Heat Transfer 121 (1999) 314–321.
[29] F.W. Dittus, L.M.K. Boelter, Heat transfer automobile radiators of the tubular type, University of California Publications in Engineering 2 (1930) 443–461.